Electronic Supplementary Material

Interface-modulated approach toward multilevel metal oxide nanotubes for lithium-ion batteries and oxygen reduction reaction

Jiashen Meng[1,§], Chaojiang Niu[1,§], Xiong Liu[1], Ziang Liu[1], Hongliang Chen[2], Xuanpeng Wang[1], Jiantao Li[1], Wei Chen[1], Xuefeng Guo[2] (✉), and Liqiang Mai[1] (✉)

[1] *State Key Laboratory of Advanced Technology for Materials Synthesis and Processing, Wuhan University of Technology, Wuhan 430070, China*

[2] *Center for Nanochemistry, Beijing National Laboratory for Molecular Sciences, State Key Laboratory for Structural Chemistry of Unstable and Stable Species, College of Chemistry and Molecular Engineering, Peking University, Beijing 100871, China*

[§] *These authors contributed equally to this work.*

Supporting information to DOI 10.1007/s12274-016-1130-x

Table S1 The viscosity (η) and average molecular weight (M_η) of HMW-PVA, MMW-PVA, and LMW-PVA, respectively

	η	M_η
HMW-PVA	0.768	52,065
MMW-PVA	0.535	32,330
LMW-PVA	0.077	2,513

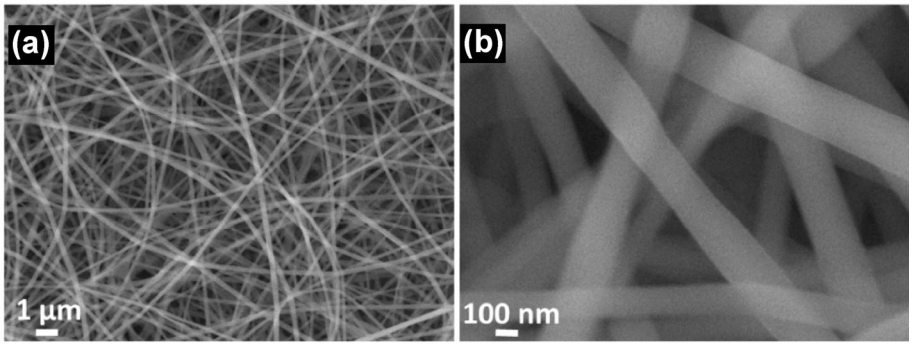

Figure S1 (a) and (b) SEM images of composite nanowires after electrospinning.

Address correspondence to Liqiang Mai, mlq518@whut.edu.cn; Xuefeng Guo, guoxf@pku.edu.cn

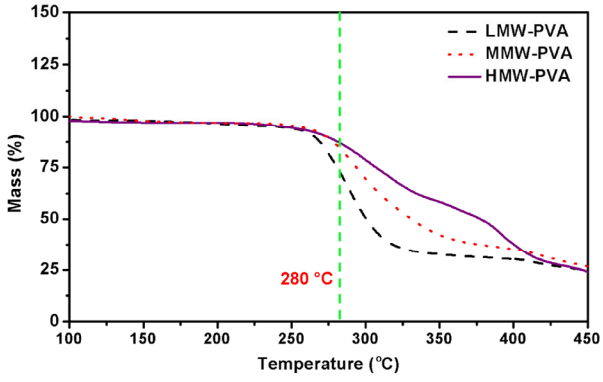

Figure S2 TG curves of LMW-PVA, MMW-PVA, and HMW-PVA in air, respectively.

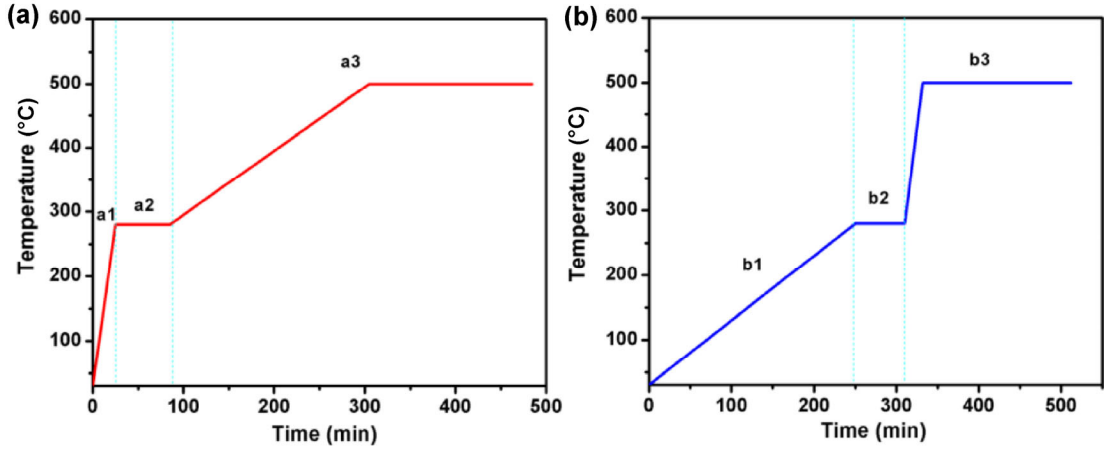

Figure S3 Controllable heat treatment curves of shrinkable wire-in-tube (a) and tube-in-tube nanotubes (b), corresponding to the schematic illustrations, respectively.

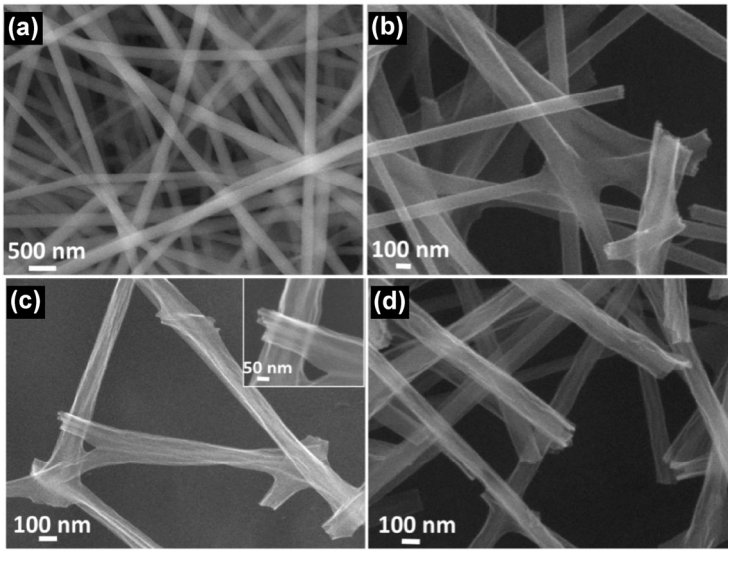

Figure S4 The formation process of shrinkable $CoMn_2O_4$ wire-in-tube nanotubes. (a) SEM image of composite nanowires after electrospinning. (b) SEM image of electrospun nanofibers when heated to 280 ˚C at 10 ˚C·min^{-1} in air. (c) SEM image of intermediate product when held at 280 ˚C for 1 h in air, inset of (c) is the corresponding magnified SEM image. (d) SEM image of shrinkable metal oxide wire-in-tube nanotubes when heated to 500 ˚C at 1 ˚C·min^{-1} and kept at 500 ˚C for 3 h in air.

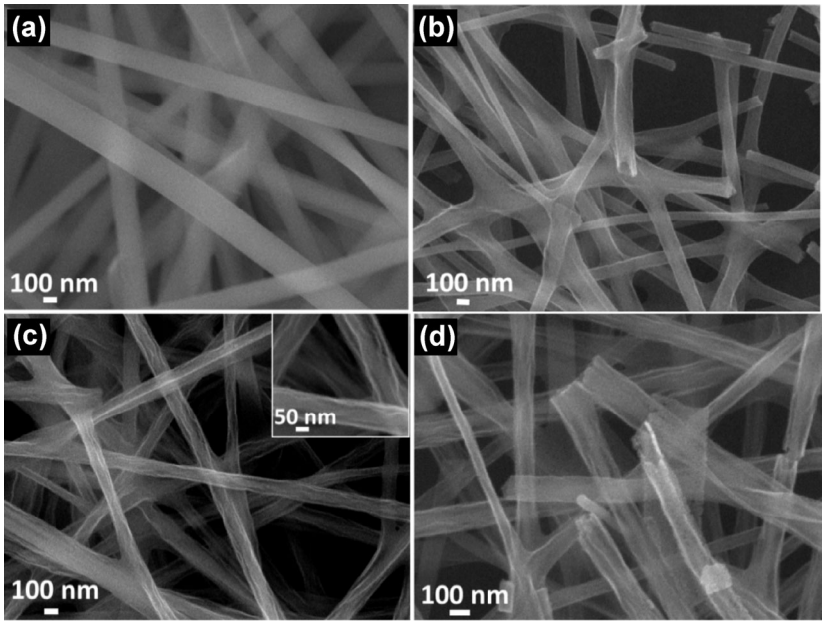

Figure S5 The formation process of shrinkable $CoMn_2O_4$ tube-in-tube nanotubes. (a) SEM image of composite nanowires after electrospinning. (b) SEM image of electrospun nanofibers when heated to 280 ˚C at 1 ˚C·min^{-1} in air. (c) SEM image of intermediate product when held at 280 ˚C for 1 h in air, inset of (c) is the corresponding magnified SEM image. (d) SEM image of shrinkable metal oxide tube-in-tube nanotubes when heated to 500 ˚C at 10 ˚C·min^{-1} and kept at 500 ˚C for 3 h in air.

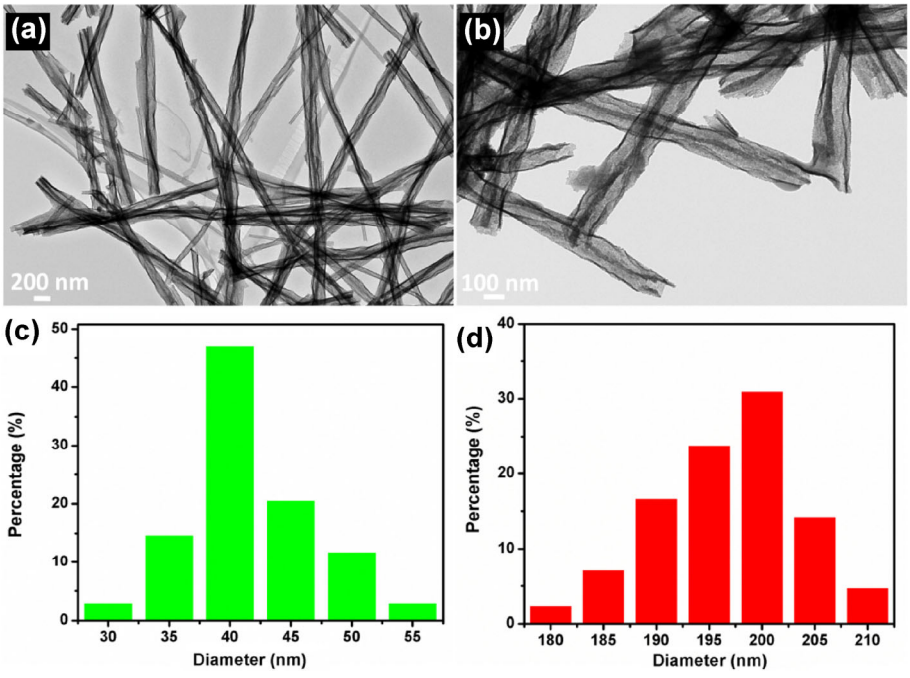

Figure S6 ((a) and (b)) TEM images of shrinkable $CoMn_2O_4$ wire-in-tube nanotubes. The diameter distributions of different inner wires (c) and outer tubes (d).

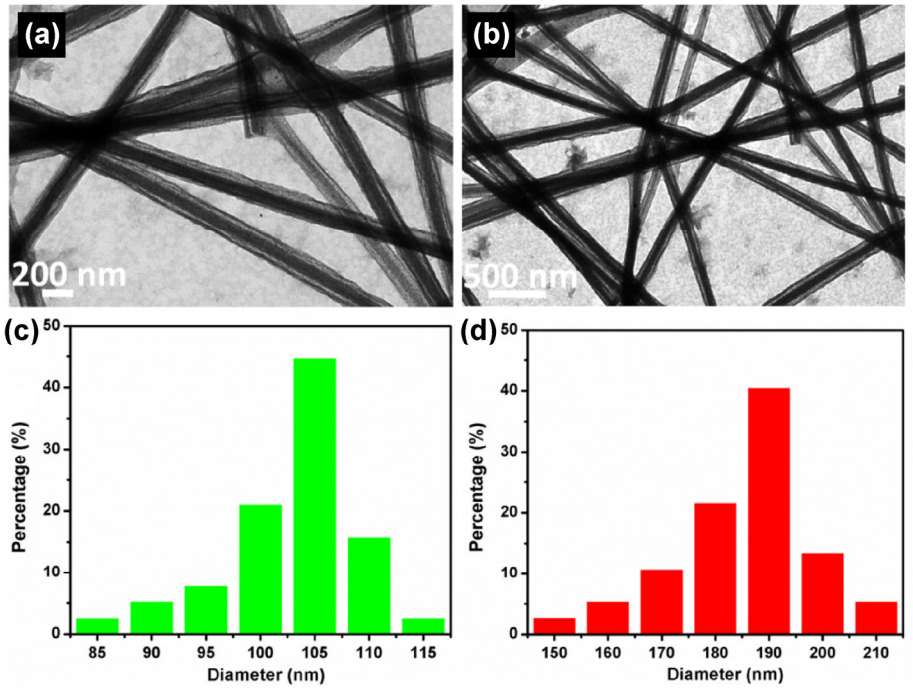

Figure S7 (a) and (b) TEM images of shrinkable $CoMn_2O_4$ tube-in-tube nanotubes. The diameter distributions of different inner tubes (c) and outer tubes (d).

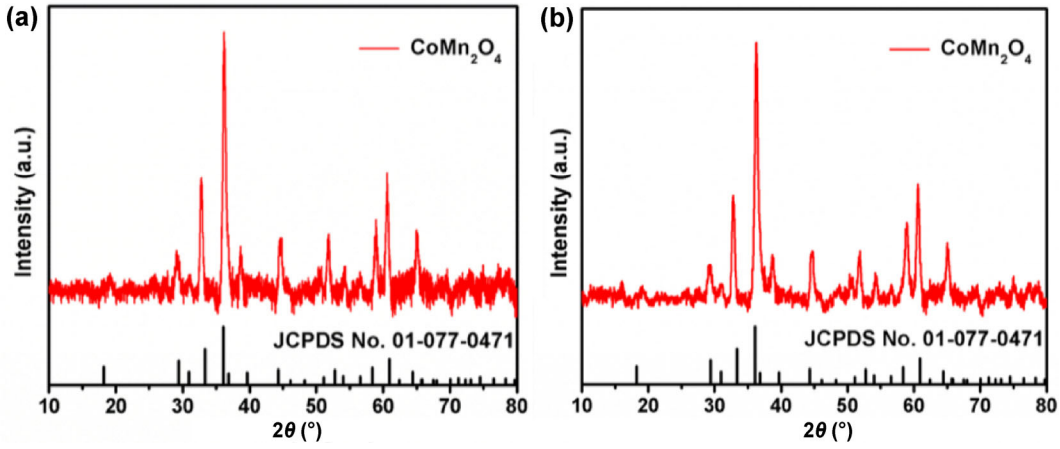

Figure S8 XRD patterns of shrinkable $CoMn_2O_4$ wire-in-tube (a) and tube-in-tube (b) nanotubes.

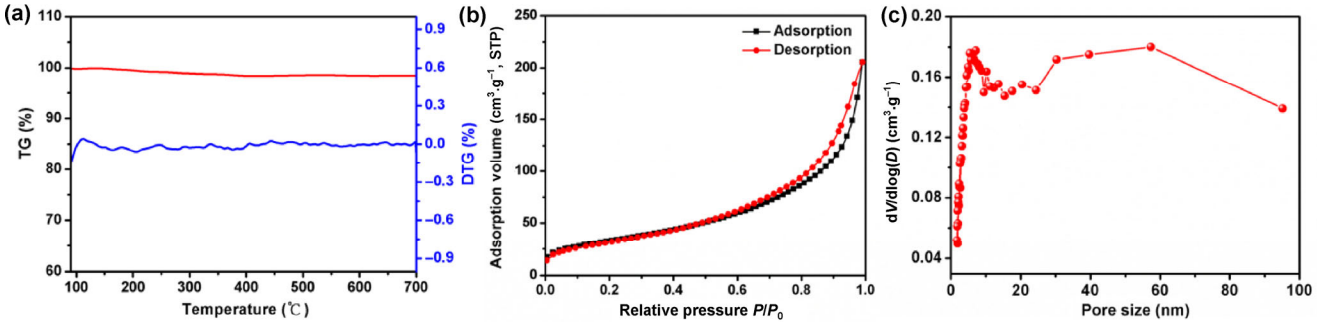

Figure S9 TGA curve (a), N_2 adsorption–desorption isotherms (b), and the pore size distribution curve (c) of shrinkable $CoMn_2O_4$ tube-in-tube nanotubes.

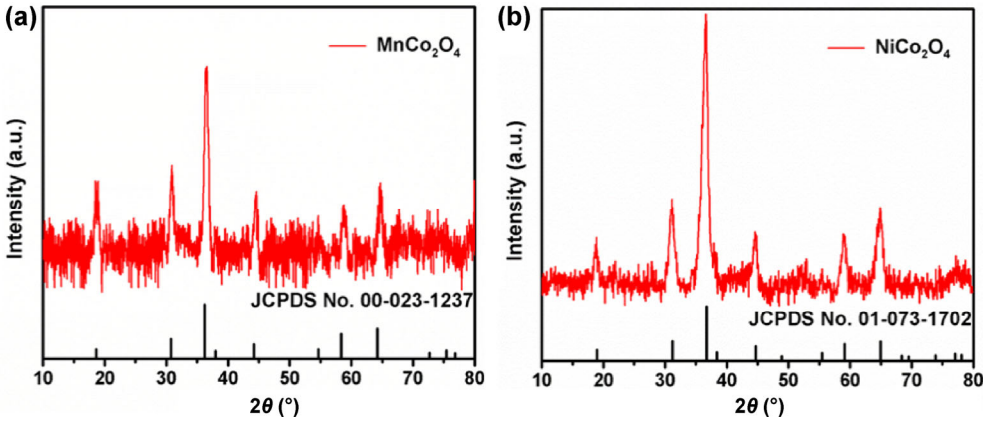

Figure S10 XRD patterns of shrinkable $MnCo_2O_4$ (a) and $NiCo_2O_4$ (b) wire-in-tube and tube-in-tube nanotubes.

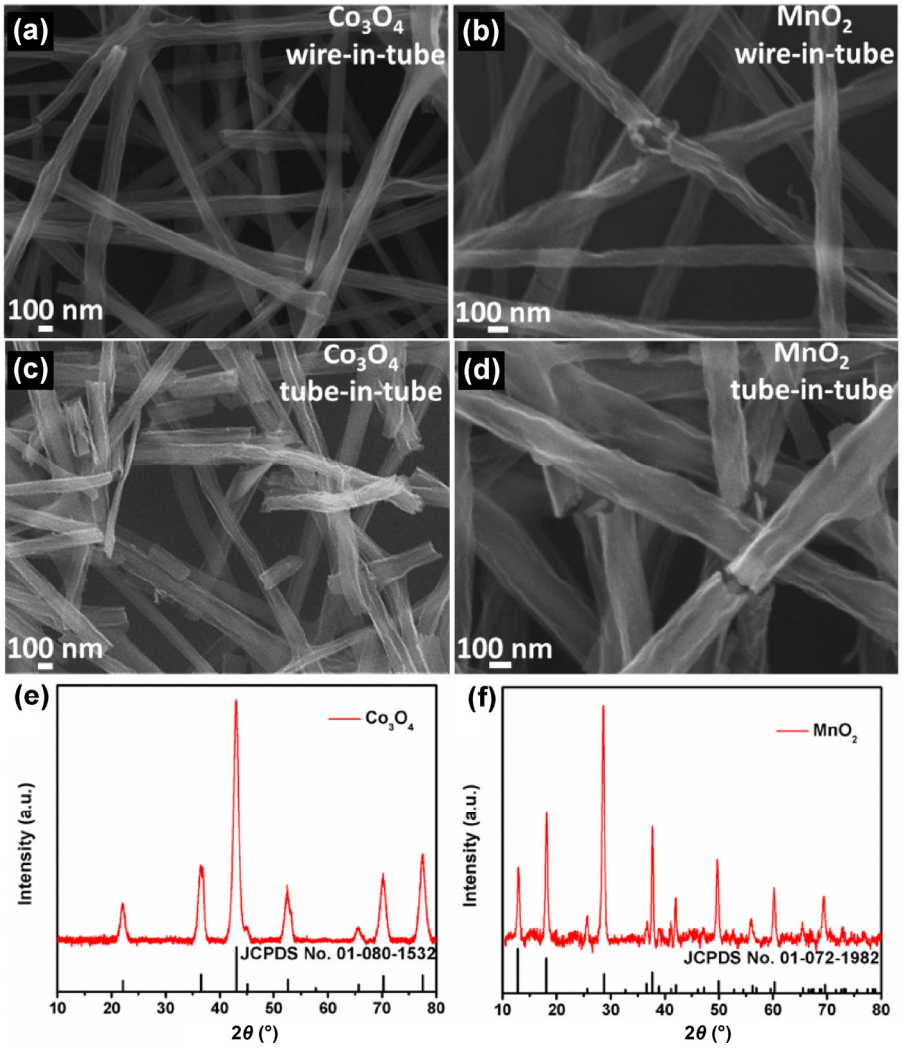

Figure S11 SEM images (a)–(d) and XRD patterns ((e) and (f)) of shrinkable Co_3O_4 and MnO_2 wire-in-tube ((a) and (b)) and tube-in-tube ((c) and (d)) nanotubes, respectively.

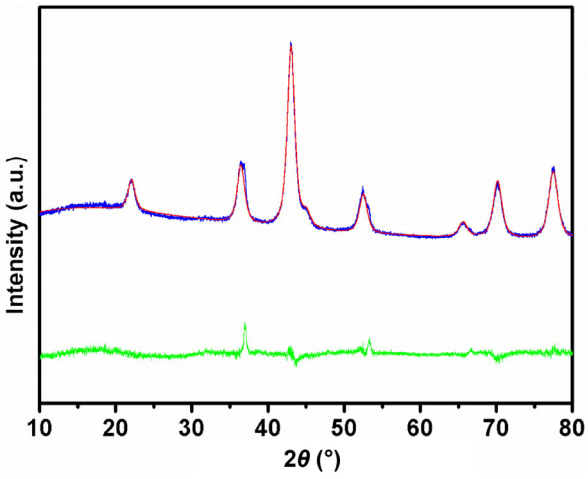

Figure S12 The Rietveld plot for shrinkable Co_3O_4 wire-in-tube nanotubes. The blue, red, and green solid lines indicate the observed, calculated patterns and their difference, respectively.

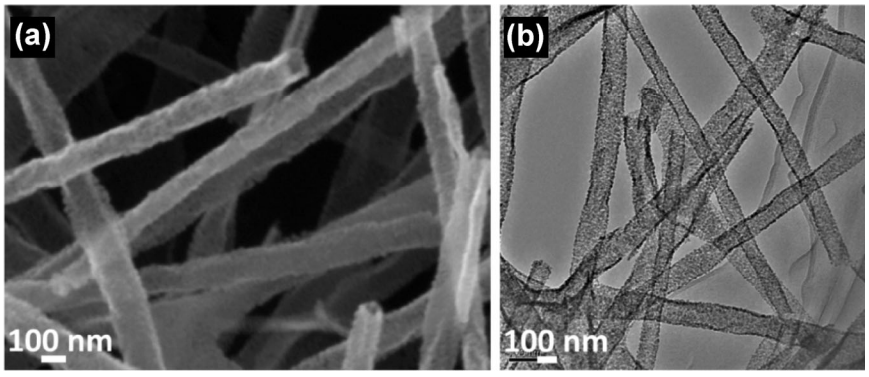

Figure S13 SEM image (a) and TEM (b) image of $CoMn_2O_4$ nanotubes.

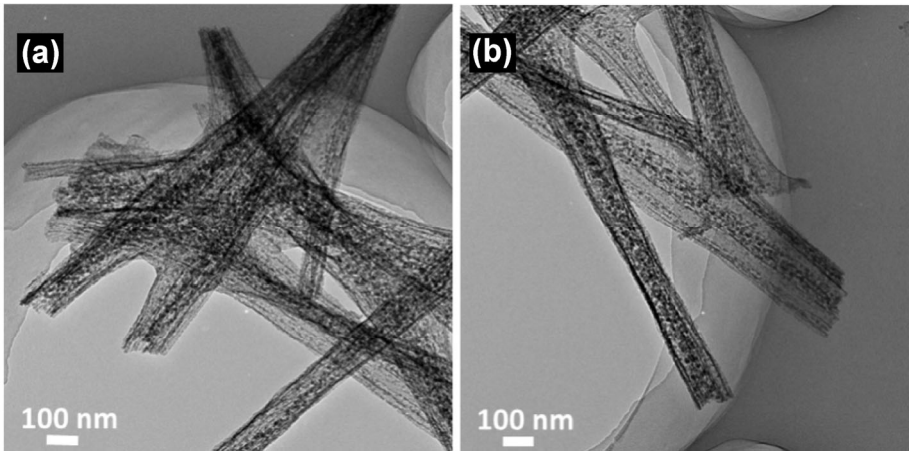

Figure S14 (a) and (b) TEM images of $CoMn_2O_4$ multishelled nanotubes.

Table S2 Crystalline sizes of the samples with different concentration based on the Scherrer formula

Samples	(*hkl*)	2θ (°)-actual	*d* (Å)	2θ (°)-PDF	FHWM (°)	Crystalline size (nm)
Co_3O_4 (3.0 mmol)	111	21.940	4.7005	22.176	0.669	14.6
	220	36.225	2.8773	36.608	0.767	13.1
	311	42.975	2.4420	43.217	0.777	13.2
	400	52.525	2.0215	52.737	0.737	14.4
Co_3O_4 (4.5 mmol)	111	22.285	4.6286	22.176	0.781	13.1
	220	36.580	2.8502	36.608	0.805	12.4
	311	43.135	2.4333	43.217	0.819	12.5
	400	52.545	2.0208	52.737	0.89	11.9
Co_3O_4 (6.0 mmol)	111	22.430	4.6154	22.176	0.875	11.0
	220	36.670	2.8424	36.608	0.875	11.4
	311	43.275	2.4237	43.217	0.844	12.1
	400	52.780	2.0124	52.737	0.835	12.7

$$D = K\lambda/B\cos(\theta)$$

The Scherrer formula can be employed to estimate the average crystallite size by XRD measurements. Where D is the average crystallite diameter, K is the Scherrer constant (a typical value is 0.9), λ is the X-ray wavelength (Cu Kα, λ = 1.5418 Å), B is the 2θ XRD peak breadth (FHWM in radians), while θ is the Bragg angle.

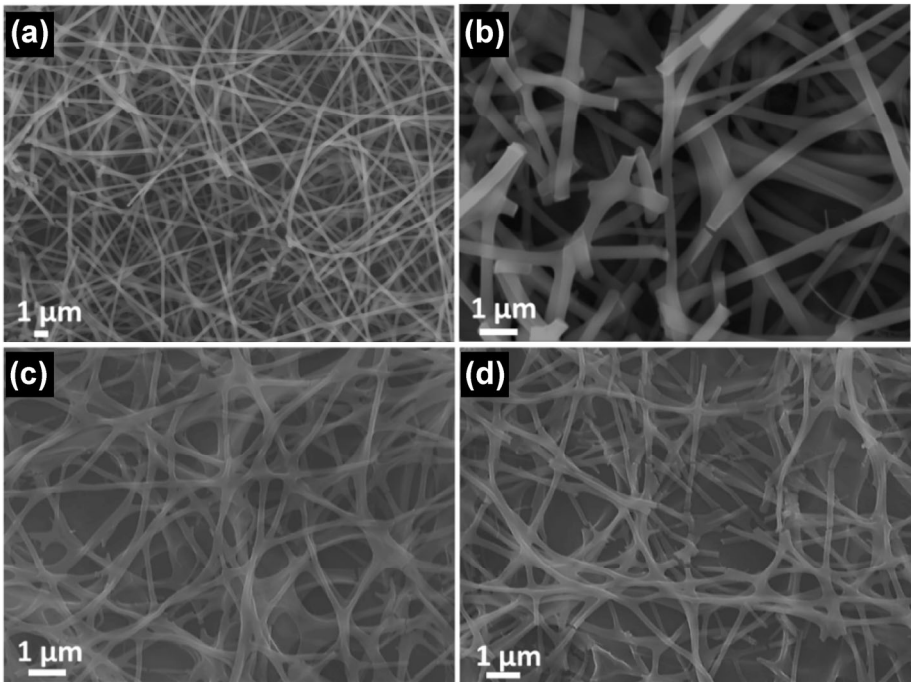

Figure S15 (a) and (b) SEM images of composite nanowires after electrospinning by using single PVA. (c) and (d) SEM images of $CoMn_2O_4$ nanowires after differernt heat treatment process.

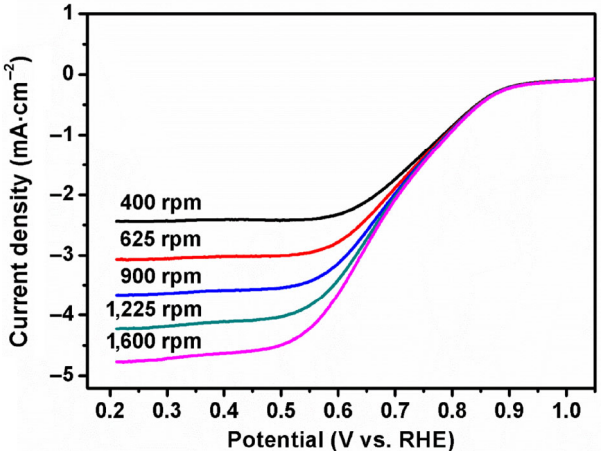

Figure S16 LSV curves of shrinkable $CoMn_2O_4$ tube-in-tube nanotubes in O_2-saturated 0.1 M KOH at a scan rate of 5 mV·s^{-1} and different rotation rates.

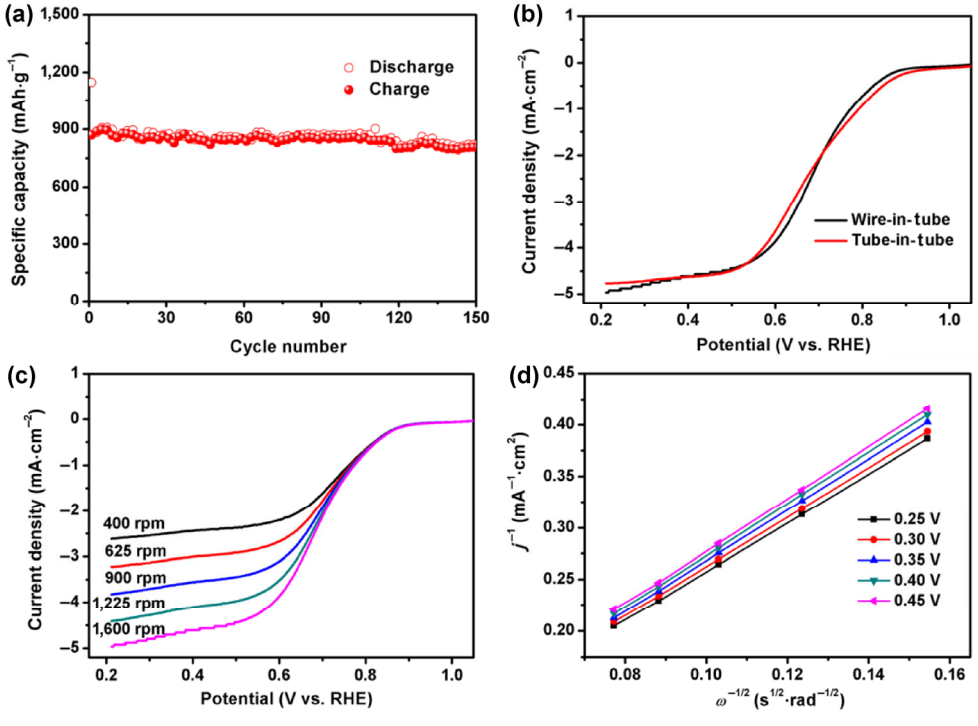

Figure S17 Electrochemical performance of shrinkable $CoMn_2O_4$ wire-in-tube nanotubes in LIB and ORR. (a) Cycling performance at current density of 200 mA·g^{-1} in LIB. (b) LSV curves of shrinkable $CoMn_2O_4$ wire-in-tube (black line) and tube-in-tube (red line) nanotubes in O_2-saturated 0.1 M KOH at a scan rate of 5 mV·s^{-1} and 1,600 rpm. (c) LSV curves in O_2-saturated 0.1 M KOH at 5 mV·s^{-1} and different rotation rates. (d) The corresponding K–L plots at different potentials.

In Fig. S17(a), shrinkable $CoMn_2O_4$ wire-in-tube nanotubes as a lithium-ion battery anode exhibit excellent cycling performance after 150 cycles at 200 mA·g^{-1}, with a 93% capacity retention. From LSV curves in the rotating disk electrode experiments, the onset potential and diffusion-limiting current of shrinkable $CoMn_2O_4$ wire-in-tube nanotubes are similar with those of shrinkable $CoMn_2O_4$ tube-in-tube nanotubes in Fig. S17(b). Rotating disk electrode experiments at different rotating rates are carried out (Fig. S17(c)) and the corresponding kinetic parameters are analyzed with the K–L equation (Fig. S17(d)). The average value of electron transfer numbers below 0.5 V is 3.7. In a word, shrinkable $CoMn_2O_4$ wire-in-tube nanotubes also

possess excellent performance in LIB and ORR, which are similar with shrinkable $CoMn_2O_4$ tube-in-tube nanotubes.

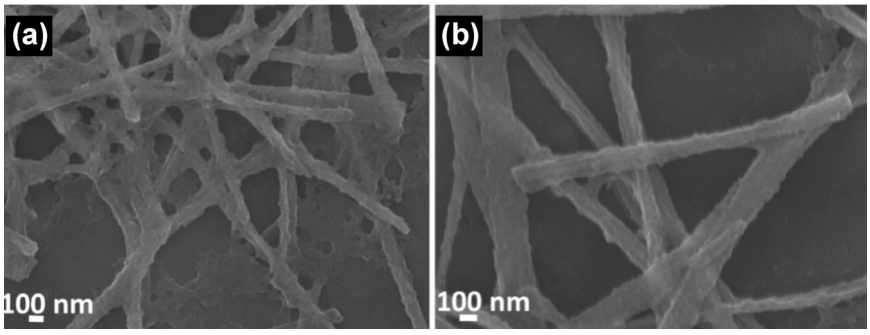

Figure S18 (a) and (b) SEM images of shrinkable $CoMn_2O_4$ tube-in-tube nanotubes after 100 cycles at the current density of 200 $mA \cdot g^{-1}$.

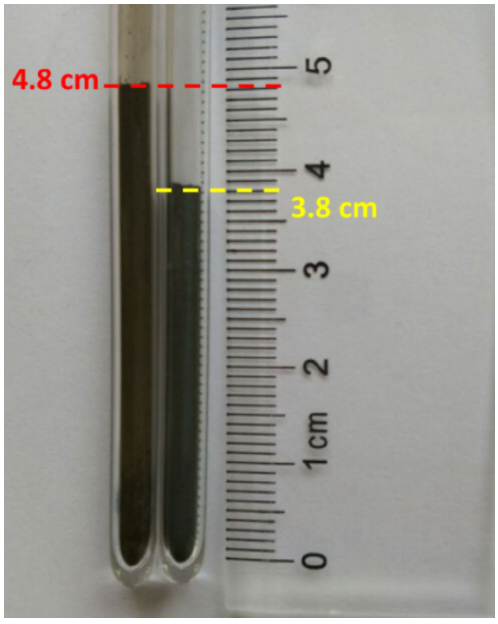

Figure S19 Digital photo shows 200 mg of MnO_2 tube-in-tube nanotubes (left) or shrinkable MnO_2 tube-in-tube nanotubes (right) in quartz tubes with inner diameter of about 6 mm, which are fully grinded.

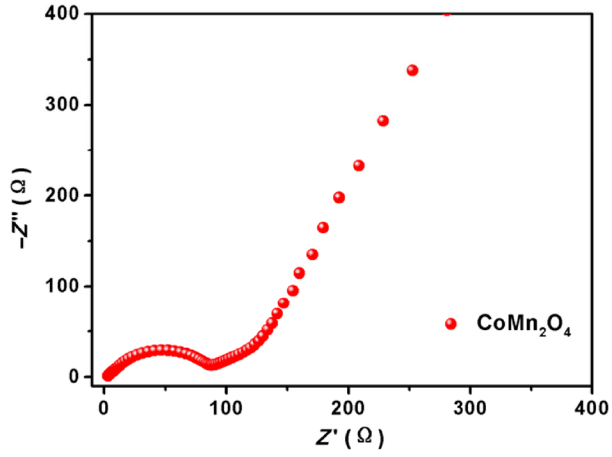

Figure S20 Alternating-current impedance plot of shrinkable $CoMn_2O_4$ tube-in-tube nanotubes.

Table S3 The comparisons of our work and previously reports in different nanostructured $CoMn_2O_4$ for lithium-ion battery

Morphology	Voltage range (V)	Current density ($mA \cdot g^{-1}$)	Cycle number	Residual capacity ($mAh \cdot g^{-1}$)	Capacity retention	Reference
$CoMn_2O_4$ tube-in-tube nanotubes	0.01–3	200 2,000	140 500	923 503	98% 89%	Our work
Hollow $CoMn_2O_4$ microspheres	0.01–3	1,000	50	585	73%	[S1]
Hollow $CoMn_2O_4$ nanofibers	0.01–3	400	100	506	63%	[S2]
$MnCo_2O_4$ microspheres	0.01–3	400	200	553	58%	[S3]
Core–shell ellipsoidal $MnCo_2O_4$	0.01–3	100	70	750	88%	[S4]
Hollow $CoMn_2O_4$ microspheres	0.01–3	200	25	706	77%	[S5]
$CoMn_2O_4$ nanorods	0.01–3	200	100	510	57%	[S6]
Yolk-shell $CoMn_2O_4$ microspheres	0.01–3	800	40	579	80%	[S7]
$CoMn_2O_4$ nanotubes	0.01–3	100	50	800	88%	[S8]
Double-shelled $CoMn_2O_4$ microcubes	0.01–3	200	50	624	76%	[S9]

References

[S1] Zhang, L. X.; Wang, Y. L.; Jiu, H. F.; Zheng, W. H.; Chang, J. X.; He, G. F. Controllable synthesis of spinel nano-$CoMn_2O_4$ via a solvothermal carbon templating method and its application in lithium ion batteries. *Electrochim. Acta* **2015**, *182*, 550–558.

[S2] Yang, G. R.; Xu, X.; Yan, W.; Yang, H. H.; Ding, S. J. Single-spinneret electrospinning fabrication of $CoMn_2O_4$ hollow nanofibers with excellent performance in lithium-ion batteries. *Electrochim. Acta* **2014**, *137*, 462–469.

[S3] Fu, C. C.; Li, G. S.; Luo, D.; Huang, X. S.; Zheng, J.; Li, L. P. One-step calcination-free synthesis of multicomponent spinel assembled microspheres for high-performance anodes of Li-ion batteries: A case study of $MnCo_2O_4$. *ACS Appl. Mater. Interfaces* **2014**, *6*, 2439–2449.

[S4] Huang, G. Y.; Xu, S. M.; Xu, Z. H.; Sun, H. Y.; Li, L. Y. Core–shell ellipsoidal $MnCo_2O_4$ anode with micro-/nano-structure and concentration gradient for lithium-ion batteries. *ACS Appl. Mater. Interfaces* **2014**, *6*, 21325–21334.

[S5] Li, J. F.; Xiong, S. L.; Li, X. W.; Qian, Y. T. A facile route to synthesize multiporous $MnCo_2O_4$ and $CoMn_2O_4$ spinel quasi-hollow spheres with improved lithium storage properties. *Nanoscale* **2013**, *5*, 2045–2054.

[S6] Wang, L. J.; Liu, B.; Ran, S. H.; Wang, L. M.; Gao, L. N.; Qu, F. Y.; Chen, D.; Shen, G. Z. Facile synthesis and electrochemical properties of $CoMn_2O_4$ anodes for high capacity lithium-ion batteries. *J. Mater. Chem. A* **2013**, *1*, 2139–2143.

[S7] Kim, M. H.; Hong, Y. J.; Kang, Y. C. Electrochemical properties of yolk-shell and hollow $CoMn_2O_4$ powders directly prepared by continuous spray pyrolysis as negative electrode materials for lithium ion batteries. *RSC Adv.* **2013**, *3*, 13110–13114.

[S8] Hwang, S. M.; Kim, S. Y.; Kim, J.-G.; Kim, K. J.; Lee, J.-W.; Park, M.-S.; Kim, Y.-J.; Shahabuddin, M.; Yamauchi, Y.; Kim, J. H. Electrospun manganese-cobalt oxide hollow nanofibers synthesized via combustion reactions and their lithium storage performance. *Nanoscale* **2015**, *7*, 8351–8355.

[S9] Zhou, L.; Zhao, D. Y.; Lou, X. W. Double-shelled $CoMn_2O_4$ hollow microcubes as high-capacity anodes for lithium-ion batteries. *Adv. Mater.* **2012**, *24*, 745–748.